

# Charge-carrier-type controlled superconducting dome in $\text{ZrN}_x\text{O}_y$ films

Xinbo Bai,<sup>1,2</sup> Fucong Chen,<sup>1,2</sup> Yuxin Wang,<sup>1,2</sup> Juan Xu,<sup>1,3</sup> Ruozhou Zhang,<sup>1,2</sup> Mingyang Qin,<sup>1,4</sup> Wenxin Cheng,<sup>1,2</sup> Jinsong Zhang,<sup>1,2</sup> Qiuyan Shi,<sup>1,2</sup> Xu Wang,<sup>1</sup> Beiyi Zhu,<sup>1</sup> Jie Yuan,<sup>1,3</sup> Qihong Chen,<sup>1,3</sup> Jian Kang,<sup>5</sup> Kun Jiang,<sup>1,2</sup> Jiangping Hu,<sup>1</sup> Yangmu Li,<sup>1,2,\*</sup> Kui Jin,<sup>1,2,6,\*</sup> and Zhongxian Zhao<sup>1,6</sup>

<sup>1</sup>Beijing National Laboratory for Condensed Matter Physics, Institute of Physics, Chinese Academy of Sciences, Beijing 100190, People's Republic of China

<sup>2</sup>School of Physical Sciences, University of Chinese Academy of Sciences, Beijing 100049, People's Republic of China

<sup>3</sup>School of Physics and Technology, Wuhan University, Wuhan 430072, People's Republic of China

<sup>4</sup>Department of Physics, Southern University of Science and Technology, Shenzhen 518055, People's Republic of China

<sup>5</sup>School of Physical Science and Technology, ShanghaiTech University, Shanghai 201210, People's Republic of China

<sup>6</sup>Songshan Lake Materials Laboratory, Dongguan, Guangdong 523808, People's Republic of China



(Received 17 May 2023; accepted 24 August 2023; published 12 September 2023)

Modifying the normal state charge carriers and the related Fermi surface can significantly affect a material's superconducting state. The recently discovered superconducting dome as a function of chemical concentration in transition metal nitrides provides a promising platform for achieving such control. However, this effort was hindered by synthesis techniques that cannot stabilize the material's structure in the presence of a significant number of nitrogen vacancies. In this study, we employed oxygen-assisting nitrogen gas flow with radio frequency magnetron sputtering to stabilize the crystal structure of nitrogen-deficient zirconium nitride thin films and explore the impact of normal state charge carrier types on the superconducting state. Our electrical and thermoelectrical transport measurements indicate a fine-tuning of the superconducting transition temperature,  $T_c$ , through a shift from hole-type to electron-type charge carriers. Additionally, a concurrent strain release, reflected in the change of the film's crystal orientation, is observed in the process.

DOI: [10.1103/PhysRevMaterials.7.094801](https://doi.org/10.1103/PhysRevMaterials.7.094801)

## I. INTRODUCTION

The physical properties of a superconducting state are profoundly affected by the normal state charge carriers from which Cooper pairs are formed. This phenomenon is particularly prevalent in superconductors with complex phase diagrams, where competing states coexist with close free energies [1–9]. By means of modifying material structures and chemical ratios, crystal field and band structure evolve, leading to an enhancement or suppression of superconductivity. The recent discovery of a superconducting dome in transition metal nitrides [9] offers a favorable opportunity in realizing the regulation of superconducting transition temperature  $T_c$  via modifications in the band structure. Despite being known for over three decades, the nature of superconductivity in these materials is still a topic of debate, e.g., the density of states at the Fermi surface [10] and electron-phonon coupling strength [11] are too low to explain their relatively high  $T_c$ . For materials such as  $\text{ZrN}_x$  [9,12–15],  $\text{HfN}_x$  [16,17],  $\text{NbN}_x$  [18–24],  $\text{TaN}_x$  [25,26],  $\text{TiN}_x$  [27–29], and  $\text{VN}_x$  [30–34], nitrogen content is observed to have a great influence on superconductivity. Studies on  $\text{ZrN}_x$  [9,35] suggest that the superconducting transition is governed by a combination of the electron-phonon coupling strength and the number of mobile carriers. While continuously lowering the

amount of nitrogen content can serve as an effective method to reduce the number of charge carriers, it also destabilizes the crystal structure [9], resulting in difficulties for detailed studies.

Extensive research has been conducted over the years on the synthesis [36,37] and electrical transport properties [38–41] of  $\text{ZrN}_x\text{O}_y$ . Oxygen-assisting crystal synthesis of superconducting transition metal nitrides has multiple benefits: oxygen (O) and nitrogen (N) ions have different valences, and replacing nitrogen with oxygen allows control of mobile carriers while keeping crystal structure stable; introducing oxide and nitride domains in crystal film in extreme growth conditions (i.e., the combined N/O concentration is much less than or far above that of Zr) offers an outlet of interface strain that otherwise can destroy the overall crystal structure. We found that by employing oxygen-assisting nitrogen gas flow with radio frequency magnetron sputtering,  $\text{ZrN}_x\text{O}_y$  with previously challenging chemical compositions can be stabilized, even with  $\sim 40\%$  nominal total N and O vacancies.

To estimate the effect of replacing N by O atoms and compare it with that purely induced by the changing of N concentration, we apply density functional theory (DFT) calculation with the projector augmented wave (PAW) method and a generalized gradient approximation (GGA) (the same as in Ref. [9]). The band structures of  $\text{ZrN}_x\text{O}_y$  are obtained by virtual-crystal approximation (VCA). We found that this method overestimates the effect of N vacancy in modifying lattice constants. As a result, we achieve energy minimization

\*Corresponding authors: yangmuli@iphy.ac.cn; kuijin@iphy.ac.cn

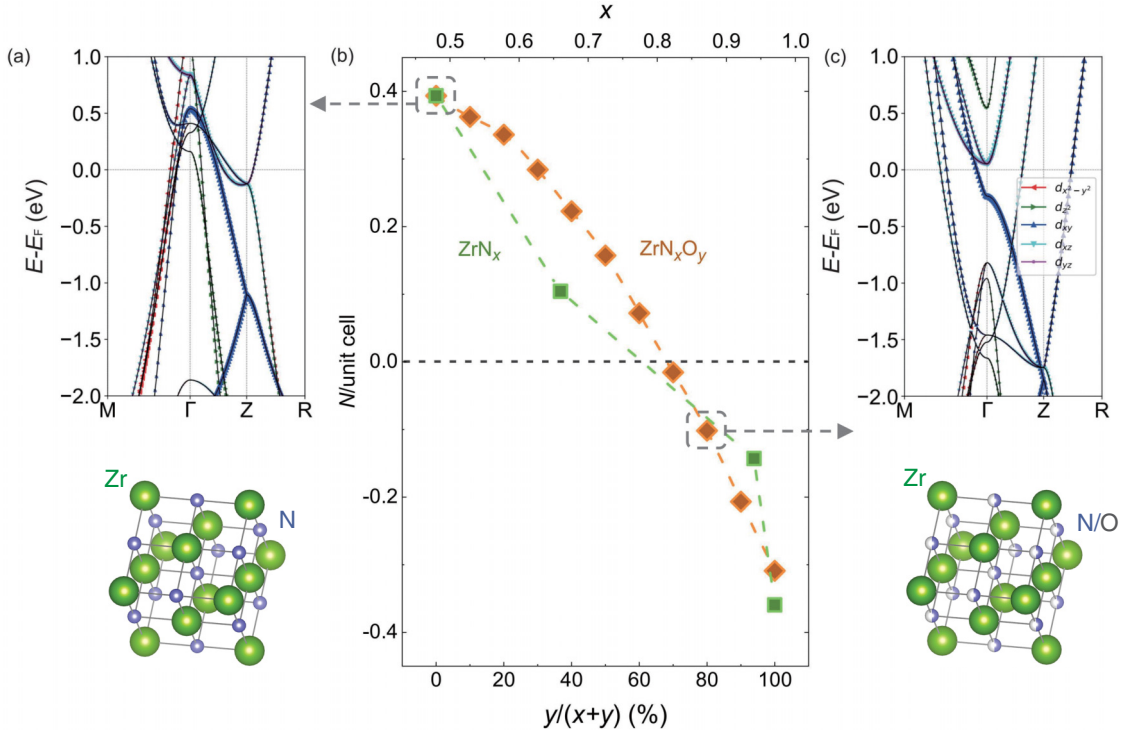


FIG. 1. Band structure and qualitative estimation of the number of charge carriers. (a) Band structure of  $y/(x+y) = 0$   $\text{ZrN}_x\text{O}_y$ , where hole bands are observed near  $\Gamma$ . (b) The total number of charge carriers ( $N$ ) per unit cell for  $\text{ZrN}_x$  (green square) and  $\text{ZrN}_x\text{O}_y$  (orange diamonds). The hole-to-electron carrier type transition occurs at  $x \sim 0.75$  for  $\text{ZrN}_x$  and at  $y/(x+y) \sim 0.7$  for  $\text{ZrN}_x\text{O}_y$ . Here,  $x+y$  is set to a constant for various values of  $y/(x+y)$ . (c) Band structure of  $\text{ZrN}_x\text{O}_y$   $y/(x+y) \sim 0.7$ , where electron bands are observed near  $\Gamma$ .

by relaxing the lattice constants and atomic coordinates to obtain the appropriate crystal structure. For simplicity, we obtain the effective N content by normalizing the  $c$ -axis lattice constants from DFT calculation to experimental ones, which allows direct comparison between the two.

The total charge carriers for extremely nitrogen-deficient  $\text{ZrN}_x$  are found to be the hole type. By increasing the N content, the carrier type changes to the electron dominate near  $x \sim 0.75$ . A similar change can be realized by replacing  $\sim 70\%$  of N by O (Fig. 1), while keeping the total N and O concentration as a constant. The change of charge carrier type is rooted in the evolution of electron bands across the Fermi surface for which oxygen and nitrogen elements in  $\text{ZrN}_x\text{O}_y$  work collaboratively. Experimental results show that the DFT calculations qualitatively capture the change of carrier type in  $\text{ZrN}_x\text{O}_y$  films.

## II. EXPERIMENTAL RESULTS

### A. Thin film growth and characterization

$\text{ZrN}_x\text{O}_y$  films were grown on the (111)-oriented MgO and silicon substrates using the radio frequency magnetron sputtering with a 99.95% Zr target. We utilized the silicon substrate solely for the purpose of calibrating the oxygen concentration of the synthesized film. The substrates were preheated to  $800^\circ\text{C}$  under a vacuum condition of  $5.0 \times 10^{-5}$  Pa before a combination of gas flow is passed into the chamber. By fixing the  $\text{N}_2$  partial pressure (0.05 Pa) and varying the  $\text{O}_2$  flow rate [0–0.52 SCCM (SCCM denotes cubic centimeter

per minute at STP)] while keeping the total pressure at 0.5 Pa (compensating Ar to maintain the total pressure), we obtained  $\text{ZrN}_x\text{O}_y$  films with a thickness of about  $1.3 \mu\text{m}$  after two 600-s sputtering sessions (presputtering and formal sputtering with the power of 200 W). To acquire a series of  $\text{ZrN}_x\text{O}_y$  films with charge carrier type from hole to electron, we first synthesized  $\text{ZrN}_x\text{O}_y$  with nominal  $x \sim 0.35$ ,  $y \sim 0.05$  (Table I), and then increased the  $\text{O}_2$  flow rate. Our end material was  $\text{ZrN}_x\text{O}_y$  with  $x \sim 0.6$  and  $y \sim 0.4$ . As suggested by the DFT calculation, either the increase in N concentration alone or that in the  $y/(x+y)$  ratio can achieve a hole-to-electron type transition in our films. We combined the two effects to realize the transition.

Figure 2 depicts the structural and chemical characterization of  $\text{ZrN}_x\text{O}_y$  films. The atomic fractions of Zr, N, and O atoms are acquired by energy dispersive x-ray spectroscopy (EDX). To facilitate clear separation of signals from  $\text{ZrN}_x\text{O}_y$  films and substrate, the films grown on silicon substrates were used for the chemical analysis. Because EDX can only obtain results for the relative chemical ratios, we normalized our data to that of ZrN for absolute values (similar to that in Ref. [9]). Since both N and O concentrations are changing, for a simple presentation to take both into account, we used the total nominal valence of Zr,  $(3x+2y)$  to label  $\text{ZrN}_x\text{O}_y$  films.

The total nominal valence of Zr does not evolve smoothly with increasing oxygen flow during synthesis, but shows a drastic change at approximately 0.4 SCCM [Zr valence of  $\sim 1.8$ ; Figs. 2(a) and 2(b)]. This change coincides with lattice orientation transition from ZrN (111) to ZrN (200), as revealed by the x-ray diffraction spectrum (XRD) in Fig. 2(c).

TABLE I.  $\text{ZrN}_x\text{O}_y$  film information. Resistivity at Mott-Ioffe-Regel limit is calculated as  $\rho_{\text{MIR}} = \frac{\hbar}{k_F e^2}$  and  $k_F = 2\pi(\frac{3n}{8\pi})^{1/3}$ . Sheet resistance is calculated as  $R_s = \frac{\rho_{xx}}{t}$ , where  $t$  is the film thickness. \* denotes thickness measured directly from SEM cross-section image, other estimated from film grown with similar conditions. Also listed are resistivity at 300 K ( $\rho_{300\text{K}}$ ) and 50 K ( $\rho_{50\text{K}}$ ), Hall coefficient ( $R_H$ ) at 30 K, and MR fit parameter  $b_2$  at 10 K.

O <sub>2</sub> flow (SCCM)	Zr (%)	N (%)	O (%)	$x$	$y$	Zr valence	$T_{c0}$ (K)	$\rho_{\text{MIR}}$ ( $\mu\Omega$ cm)	$\rho_{300\text{K}}$ ( $\mu\Omega$ cm)	$\rho_{50\text{K}}$ ( $\mu\Omega$ cm)	$R_H$ ( $10^{-3}\text{ cm}^3/\text{C}$ )	$b_2$ at 10 K ( $10^{-4}/\text{T}^2$ )	$R_s$ at 50 K ( $\Omega$ )	$t$ ( $\mu\text{m}$ )
0	71.26	24.95	3.77	0.350	0.053	1.16	NA	504	414	403	0.17	0.82	2.14	1.88*
0.15	64.87	30.71	4.40	0.474	0.068	1.56	NA	284	155	151	0.03	0.73	1.19	1.26*
0.30	62.23	32.13	5.62	0.516	0.090	1.73	2.72	192	264	265	0.01	NA	2.14	1.24
0.31	61.80	32.45	5.74	0.525	0.093	1.75	5.23	NA	316	313	NA	NA	2.53	1.23*
0.32	61.76	32.47	5.76	0.526	0.093	1.76	5.66	344	233	228	-0.05	1.18	1.82	1.25
0.35	61.55	32.06	6.38	0.521	0.104	1.77	6.15	380	230	224	-0.07	NA	1.74	1.29
0.40	61.10	32.45	6.43	0.531	0.105	1.80	6.66	408	266	257	-0.09	1.81	1.90	1.35
0.42	58.61	34.05	7.33	0.581	0.125	1.99	6.88	NA	$1.67 \times 10^3$	$1.60 \times 10^3$	NA	NA	11.6	1.38
0.45	55.23	35.80	8.96	0.648	0.162	2.27	6.42	864	$4.25 \times 10^3$	$4.20 \times 10^3$	-0.87	5.45	29.8	1.41
0.46	54.14	35.03	10.82	0.647	0.200	2.34	3.78	NA	$6.21 \times 10^4$	$7.31 \times 10^4$	NA	NA	511	1.43
0.47	52.60	33.93	13.46	0.645	0.256	2.37	3.53	NA	$1.16 \times 10^5$	$1.33 \times 10^5$	NA	9.47	924	1.44*
0.48	52.54	33.25	14.20	0.633	0.270	2.43	2.82	NA	$2.06 \times 10^5$	$2.63 \times 10^5$	NA	NA	$1.83 \times 10^3$	1.44
0.50	52.23	31.89	15.86	0.611	0.304	2.44	2.93	938	$2.07 \times 10^5$	$2.55 \times 10^5$	-1.11	9.63	$1.77 \times 10^3$	1.44*
0.52	50.01	30.49	19.48	0.610	0.390	2.61	NA	NA	$2.06 \times 10^7$	$5.18 \times 10^7$	NA	NA	$3.57 \times 10^5$	1.45

Such a change of crystal orientation in transition metal nitrides has been reported in the previous studies [42,43]. Since the ZrN (111) plane at the substrate interface has the lowest strain energy and the ZrN (200) plane has the lowest surface energy, the actual orientation of the film depends on the competition between the two [44]. With an increasing oxygen and nitrogen concentration, the orientation-averaged strain energy can be released, and surface energy becomes the dominating factor. Concurrently, we observe the appearance of  $\text{ZrO}_2$  structure peaks, which may induce domain separations that facilitate the above process. A typical reciprocal space mapping (RSM) of  $\text{ZrN}_x\text{O}_y$  films (Zr valence of  $\sim 1.76$ ) is plotted in Fig. 2(d), showing an epitaxial growth. The cross-section image in Fig. 2(e) captured by scanning electron microscope (SEM) of a  $\text{ZrN}_x\text{O}_y$  film with a Zr valence of 1.56 shows a thickness of  $\sim 1.26\text{ }\mu\text{m}$  (thicknesses of other films are listed in Table I). From the acquired SEM surface topographies in Fig. 2(f), it is evident that when the Zr valence is low (e.g., 1.16,  $x+y \sim 0.4$  and thus  $\sim 60\%$  nominal total N and O vacancies), the surface appears uneven with irregular crystal domains. However, as the Zr valence increases (e.g.,  $\sim 1.76$ ,  $x+y \sim 0.6$ ,  $\sim 40\%$  nominal total N and O vacancies), the film's surface becomes relatively smooth. Further increasing the Zr valence to 2.61 (approximately no N and O vacancies) results in some precipitates on the film's surface.

Characterizations of superconductivity in  $\text{ZrN}_x\text{O}_y$  films are presented in Fig. 3. Figure 3(a) shows the temperature-dependent electrical resistivity  $\rho_{xx}$  of  $\text{ZrN}_x\text{O}_y$  films. For an increasing Zr valence, the normal state resistivity changes from  $10^2$  to  $10^8\text{ }\mu\Omega$  cm, over six orders of magnitude, and superconductivity exists when resistivity is below  $10^6\text{ }\mu\Omega$  cm. We define the temperature at which superconducting transition begins as the onset temperature ( $T_c^{\text{onset}}$ ) and the temperature at which electrical resistivity becomes zero as  $T_{c0}$ . A superconducting dome emerges when tracing  $T_c^{\text{onset}}$

and  $T_{c0}$  as a function of Zr valence. The highest  $T_c^{\text{onset}} \sim 7\text{ K}$  appears with a Zr valence of 1.99. It is noteworthy that all of our films show a resistivity upturn behavior below 40 K (even in superconducting films when the temperature is above  $T_c^{\text{onset}}$ ). The temperature at which resistivity upturn occurs ( $T_{\text{upturn}}$ ) is plotted in Fig. 3(c), and a minimum  $T_{\text{upturn}}$  exists at a Zr valence of 1.80. Above 40 K, the normal state of  $\text{ZrN}_x\text{O}_y$  films changes from a strongly insulating (SI), via a metallic ( $M$ ) state, to a resistivity upturn behavior (a strong insulation regime is characterized by a resistivity above  $10^5\text{ }\mu\Omega$  cm and  $d\rho_{xx}/dT < 0$ ; metallicity is characterized by a positive  $d\rho_{xx}/dT$ ). It is noteworthy that this upturn behavior may indicate a weak insulating state or a quantum metallic state [45,46]. Interestingly, we found that the normal state resistivity of our films near room temperature is comparable or even less than the Mott-Ioffe-Regel limit (Table I). Figure 3(d) plots the  $T_c^{\text{onset}}$  and  $T_{c0}$  as a function of the normal state  $\rho_{xx}$  at 10 K. Magnetic susceptibility of  $\text{ZrN}_x\text{O}_y$  with a Zr valence of 1.99, as shown in Fig. 3(e), demonstrates bulk superconductivity in films.

## B. Hall resistivity, Seebeck coefficient, and magnetoresistivity

Next, we performed detailed Hall effect, Seebeck coefficient, and magnetoresistivity measurements of  $\text{ZrN}_x\text{O}_y$  films to determine the charge carrier type. Hall resistivities  $\rho_{xy}$  are linearly proportional to the magnetic field, and Hall results in the normal state (30 K) are depicted in Fig. 4(a). The Hall coefficient  $R_H \equiv \rho_{xy}/(\mu_0 H) \sim 1/n$ , where  $n$  is the carrier concentration, is temperature insensitive for each film and it evolves from positive to negative values as the valence of Zr exceeds  $\sim 1.75$  [Fig. 4(b)].

The Seebeck coefficient  $S$  is linearly proportional to temperature [Fig. 4(c)]. For typical Landau Fermi liquids,  $S = \frac{\pi^2 k_B^2}{3qE_F} T$ , where  $k_B$  is the Boltzmann constant and  $q$  is the

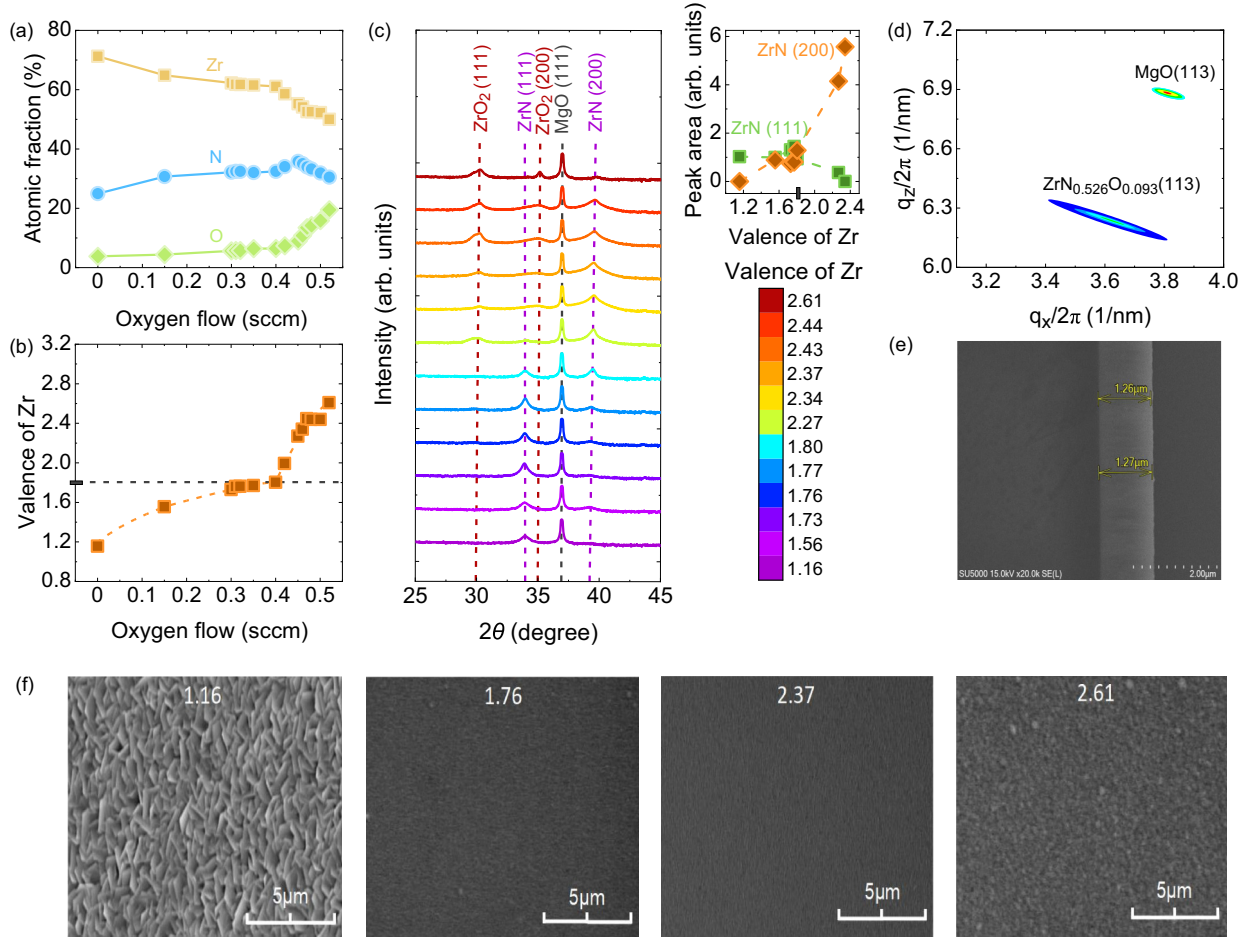


FIG. 2. X-ray and SEM characterization of ZrN<sub>x</sub>O<sub>y</sub> films. (a) Atomic fraction of Zr, N, and O as a function of oxygen flow rate. (b) Valence of Zr calculated from  $(3x + 2y)$ . (c)  $2\theta$  scan from x-ray diffraction. Here ZrN and ZrO<sub>2</sub> represent the corresponding crystal structures instead of chemical compositions. Inset shows the transition from ZrN (111) and ZrN (200) based on integrated peak intensities. (d) A typical reciprocal space mapping pattern of ZrN<sub>x</sub>O<sub>y</sub> films with Zr valence of 1.76. (e) Cross-section image captured by scanning electron microscope (SEM) of a ZrN<sub>x</sub>O<sub>y</sub> film with Zr valence of 1.56. (f) SEM surface topographies of ZrN<sub>x</sub>O<sub>y</sub> films with Zr valences of 1.16 (~60% nominal total N and O vacancies), 1.76 (~40% nominal total vacancies), 2.37 (~10% nominal total vacancies), and 2.61 (approximately no nominal N and O vacancies).

charge of a hole or an electron. The Fermi energy  $E_F$  positively correlates with the carrier concentration  $n$ , i.e.,  $E_F \propto n^{2/3}$  for three-dimensional systems, thus  $(S/T)^{-1}$  can measure the variation in  $n$ . Figure 4(d) shows temperature-independent  $S/T$  with a sign change near Zr valence  $\sim 1.75$ .

Magnetoresistivity (MR) is sensitive to the charge carrier type and the Fermi surface curvature.  $MR \equiv \frac{\rho_{xx}(H) - \rho_{xx}(H=0)}{\rho_{xx}(H=0)}$ , where  $H$  denotes the applied magnetic field. In the low field limit ( $\omega_c \tau \ll 1$ , where  $\omega_c$  is the cyclotron frequency and  $\tau$  is the scattering mean free time),  $MR \propto b_2 H^2$  for typical Fermi liquids. Since  $b_2$  of an open large Fermi surface is much less than that of a closed small Fermi surface, a dramatic increase of  $b_2$  often signifies a Fermi surface evolution [6]. We observe a two orders of magnitude increase of MR at 9 T for films with increasing Zr valence in Figs. 4(e) and 4(f), showing a change in the Fermi surface near Zr valence  $\sim 1.75$ . Due to the presence of atomic vacancies and the complex arrangement of oxygen and nitrogen atoms in ZrN<sub>x</sub>O<sub>y</sub>, obtaining reliable Fermi surface curvature for real film samples

is challenging with DFT. Therefore, we do not perform a quantitative comparison between experimental results and simulations.

### C. Phase diagram

Phase diagrams based on Hall resistivity, Seebeck coefficient, and magnetoresistivity results are summarized in Fig. 5. In Figs. 5(a)–5(c), we compare  $T_{c0}$  with estimated  $n \sim 1/R_H$ ,  $(S/T)^{-1}$ , and  $b_2$ , respectively. We note that a seeming divergence in  $n$  exists near Zr valence  $\sim 1.75$  from Hall and Seebeck results. This divergence also exists in analyses using two-band models, which introduces additional uncertainty. For simplicity, here we employ the effective one-band analysis. The rapid growth of  $b_2$ , which indicates a shift from hole-type to electron-type charge carriers, coincides with the emergence of superconductivity.

The phase diagram of ZrN<sub>x</sub>O<sub>y</sub> is depicted in Fig. 5(d), in which the color background outside of the superconducting



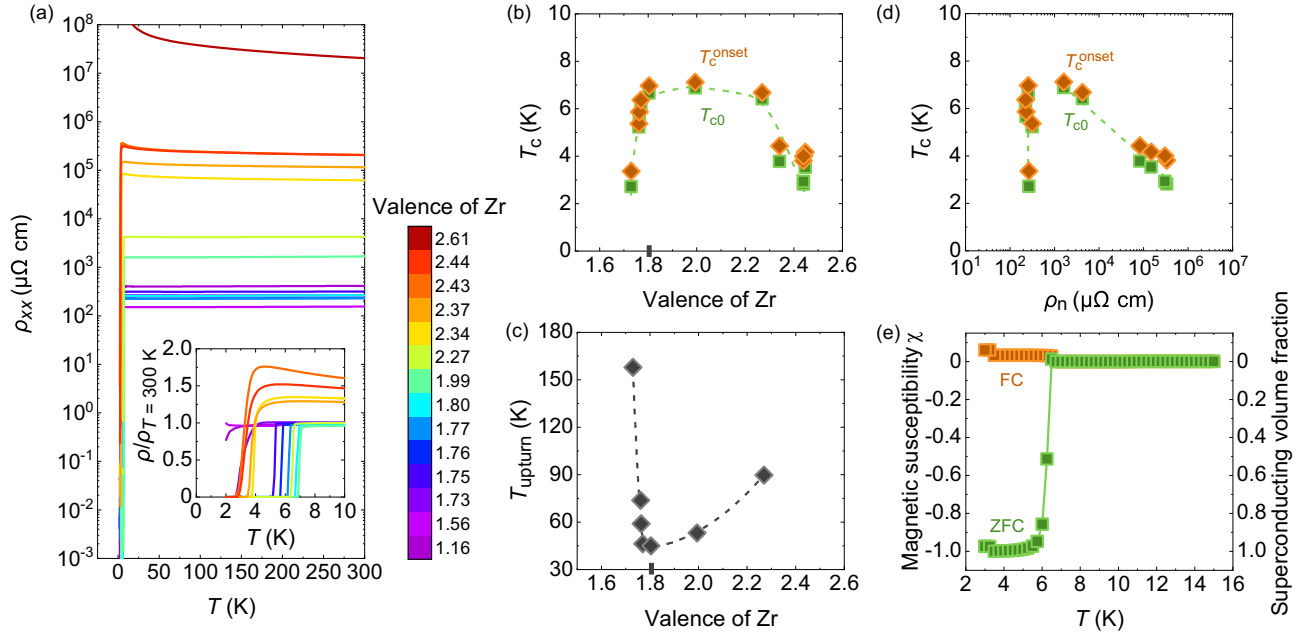


FIG. 3. Superconductivity in  $\text{ZrN}_x\text{O}_y$  films. (a) Temperature-dependent longitudinal electrical resistivity  $\rho_{xx}$ . The inset shows zoomed-in plots near the superconducting transition temperature. (b)  $T_c^{\text{onset}}$  and  $T_{c0}$  as a function of Zr valence. (c)  $T_{\text{upturn}}$  as a function of Zr valence. (d)  $T_c^{\text{onset}}$  and  $T_{c0}$  as a function of  $\rho_{xx}$  at 10 K. (e) Representative magnetic susceptibility ( $H//c$ ) and the superconducting volume fraction with Zr valence of 1.99.

dome represents the magnitude of the electrical resistivity  $\rho_{xx}$ . A resistivity upturn state and the strongly insulating state are found outside of the superconducting (SC) dome. Increasing from small Zr valence values, superconductivity appears once the transport properties are dominated by electron charge carriers (Zr valence  $> 1.75$ ), which approximately coincides with the reorientation of crystal from ZrN (111) to ZrN (200).

#### D. Resistive upper critical field

To explore the effect of charge-carrier-type change on the emergence of superconductivity in  $\text{ZrN}_x\text{O}_y$ , we study the resistive upper critical field. We measure the resistive upper critical field (defined as the magnetic field corresponding to 90% of the normal state resistivity) of  $\text{ZrN}_x\text{O}_y$  films at Zr valence of 1.76 and 1.77.  $H_{c2}$  of  $\text{ZrN}_x\text{O}_y$  films are

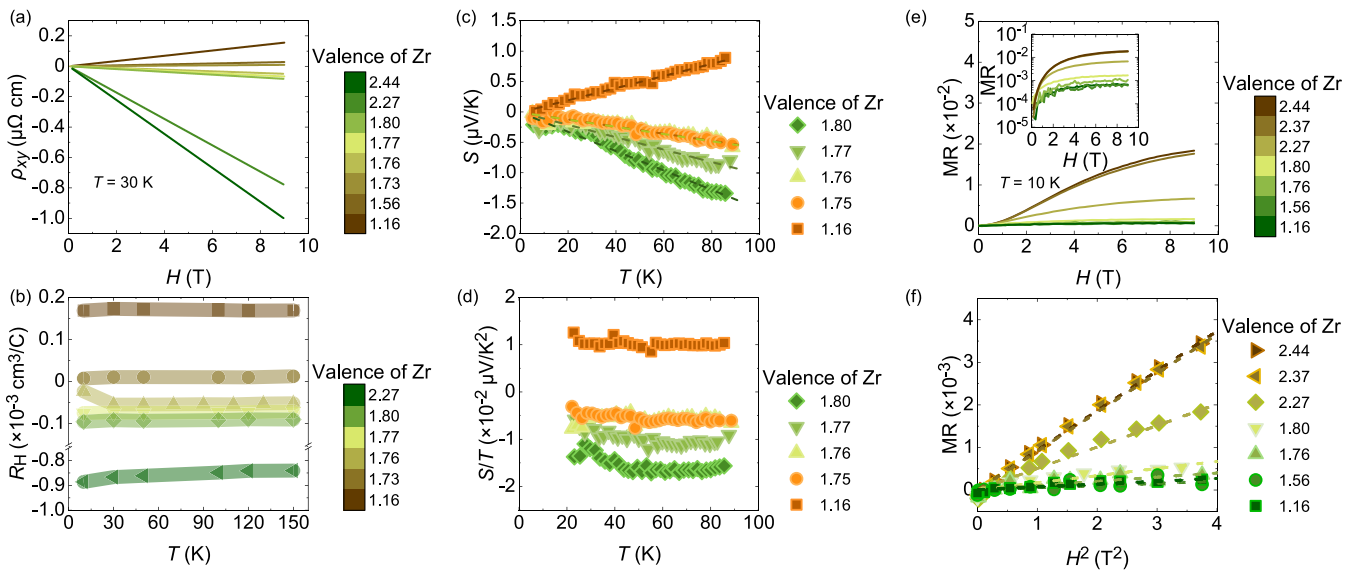


FIG. 4. Hall resistivity, Seebeck coefficient, and magnetoresistivity for  $\text{ZrN}_x\text{O}_y$  films. (a) Magnetic-field-dependent transverse resistivity  $\rho_{xy}$  at 30 K. (b) Hall coefficient  $R_H \equiv \rho_{xy}/(\mu_0 H)$ . (c) Seebeck coefficient  $S$ . (d) Seebeck coefficient divided by temperature  $S/T$ . (e) Magnetoresistivity (MR) at 10 K. The inset shows the results in a semilog scale. (f) Magnetoresistivity versus  $H^2$  and the fits at low fields.

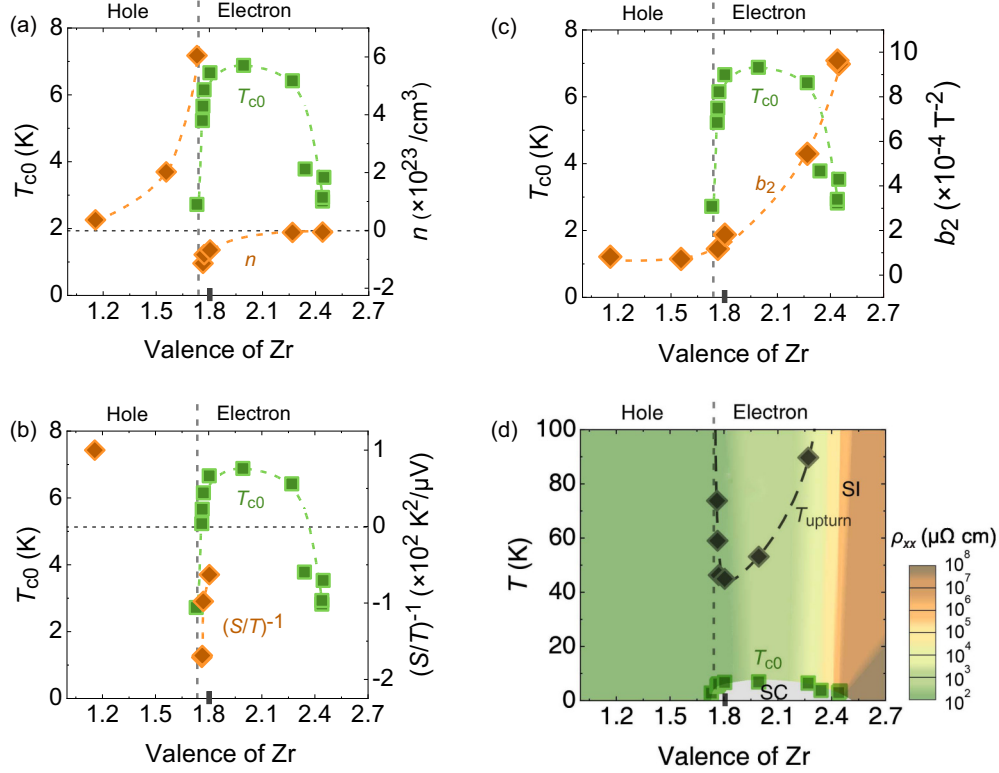


FIG. 5. Phase diagram. (a) Comparison between  $T_{c0}$  and carrier concentration  $n$  at 30 K. The positive or negative value of  $n$  only indicates that the charge carrier type is either hole or electron, and the actual numbers of carriers are their absolute values. (b) Comparison between  $T_{c0}$  and  $(S/T)^{-1}$ . Again, the positive or negative value of  $(S/T)^{-1}$  indicates that the charge carrier type is hole or electron. (c) Comparison between  $T_{c0}$  and magnetoresistivity prefactor  $b_2$  at 10 K. (d) Phase diagram of  $ZrN_xO_y$ . SI and SC denote strongly insulating and superconducting regimes, respectively.

plotted in Figs. 6(a) and 6(b), respectively. In superconducting materials with both electrons and holes, the resistive upper critical field ( $H_{c2}$ ) can be expressed by a parametric equation [an often-used Werthamer-Helfand-Hohenberg (WHH) variant model] [48,49]:

$$\ln\left(\frac{T_c}{T}\right) = \frac{1}{2} \left[ U(s) + U(\eta s) + \frac{\lambda_0}{w} \right] - \left\{ \frac{1}{4} \left[ U(s) - U(\eta s) - \frac{\lambda_-}{w} \right]^2 + \frac{\lambda_{eh}\lambda_{he}}{w^2} \right\}^{1/2},$$

$$H_{c2} = \frac{2\phi_0 T_s}{D_e} \quad \eta = \frac{D_e}{D_h},$$

$$U(s) = \psi\left(s + \frac{1}{2}\right) - \psi\left(\frac{1}{2}\right),$$

where  $\lambda_- = \lambda_{ee} - \lambda_{hh}$ ,  $\lambda_0 = (\lambda_-^2 + 4\lambda_{eh}\lambda_{he})^{1/2}$ , and  $w = \lambda_{ee}\lambda_{hh} - \lambda_{eh}\lambda_{he}$ .

$\lambda_{ee}$ ,  $\lambda_{hh}$ ,  $\lambda_{eh}$ ,  $\lambda_{he}$  are matrix elements of the superconducting coupling constants, which denote pairing strength between electron-electron, hole-hole, electron-hole, and hole-electron.

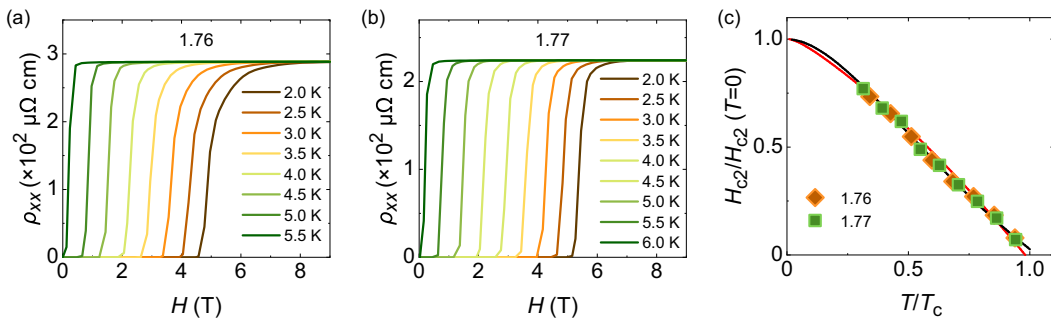


FIG. 6. Resistive upper critical field ( $H/c$ ) of  $ZrN_xO_y$  films. (a) Results for  $ZrN_xO_y$  film with Zr valence of 1.76. (b) Results for  $ZrN_xO_y$  film with Zr valence of 1.77. (c) Normalized temperature-dependent upper critical field and WHH fits. Red line indicates the best fit using the canonical WHH model and the black line indicates that using the WHH variant model.

$D_e$  and  $D_h$  are the diffusivities of electrons and holes.  $\phi_0$  is the magnetic flux quantum.  $\psi(x)$  is the digamma function. We employed both the canonical WHH [47] and its often-used variant [48,49] to fit the resistive upper critical field. For both fits, we found  $\lambda_{ee} \sim 0.7$ ,  $\lambda_{hh} \sim 0.2$ ,  $\eta \sim 0.2$ , and  $\frac{D_e}{D_h} \sim 0.2$ . For the canonical WHH model, we found  $\lambda_{eh} \sim \lambda_{he} \sim 0.5$  [red line in Fig. 6(c)], and for the WHH variant model,  $\lambda_{eh} \sim \lambda_{he} \sim 0.1$  [black line in Fig. 6(c)]. The differences and uncertainties mainly come from the unavailable data below 2 K that are inaccessible to our instrumentation. Nevertheless, both results are consistent with the emergence of superconductivity in films with the electron type of charge carriers [6,48].

### III. DISCUSSION

Our work demonstrates the electron carrier as a dominating condition to realize superconductivity in  $\text{ZrN}_x\text{O}_y$ . This result is consistent with what is observed for  $\text{ZrN}_x$  [9]. For  $\text{ZrN}_x$ , the superconductivity is entirely controlled by N content, and the superconductivity is found to be controlled by the electron-phonon coupling in the weakly insulating N deficient regime. Previous studies of ZrN also suggest a  $s$ -wave pairing symmetry [35]. From  $x \ll 1$  to  $x \sim 1$ , electron-phonon coupling strength increases and the change in superconducting transition temperature can be described by McMillan's formula [9]. The total number of carriers (Fig. 1) per unit cell changes type from a positive value (hole dominant) to negative (electron dominant) when superconductivity appears in  $\text{ZrN}_x$ . We note that Ref. [9] only calculated the number of charge carriers in Zr bands, and in this work, we calculate the total number of carriers from all bands.

It is crucial to discuss the cause of the change in carrier type. From the material synthesis perspective, in  $\text{ZrN}_x\text{O}_y$ , the significant number of atomic vacancies can lead to unstable structure, domain boundaries, and potential phase separation between Zr and  $\text{ZrN}_x$  [38–41]. Indeed, we observe uneven surface and irregular crystal domains for nominal total N and O vacancy number  $\sim 60\%$ . As shown in Fig. 2(f), with the increasing valence of Zr, the film surface quality increases and well-defined crystallization is already achieved even for films with a nominal total N and O vacancy number  $\sim 40\%$ . Near Zr valence of 1.80, transport measurements find clear evidence

of charge carrier type change and crystal orientation reorienting from ZrN(111) to (200). We note that (111) and (200) orientations of the films both belong to the same  $\text{ZrN } Fm\bar{3}m$  structure [9], and thus lattice constant relaxation and related band structure modification are likely to be responsible for the sudden transition from hole to electron dominating carriers. DFT calculation [Fig. 1(b)] indicates that the hole to electron evolution exists without the crystal reorientation. As reported in Ref. [9], the BCS paradigm can offer a basically satisfactory explanation for the evolution of superconducting transition temperature. However, various factors such as film quality, disorder, and impurities can influence the detailed aspects of superconductivity (for instance, BCS theory predicts distinct superconducting behaviors in the clean and dirty limits). Nevertheless, we believe that the primary factor governing the emergence of superconductivity is the hole-to-electron Fermi surface transition.

For transition metal nitrides in general, replacing nitrogen with oxygen can modify the valency while keeping the structure stabilized. The material synthesis technique in our work provides a promising route in realizing remarkable physics properties. For example,  $\text{ZrN}_x\text{O}_y$  can be used as low-temperature thermometers, showing high sensitivity [44,50] and low magnetoresistance [51]. Additionally, the introduction of oxygen in  $\text{CoN}_x$  has been proposed to induce magnetic transitions and potentially lead to the emergence of superconductivity [52]. Applying our method can facilitate the exploration of other transition metal nitrides. A similar method may even provide a viable approach for synthesizing bulk transition metal nitroxides, given that oxygen is able to permeate into the bulk crystal (e.g., synthesis under high-pressure conditions).

### ACKNOWLEDGMENTS

This work was supported by the National Key Basic Research Program of China (Grant No. 2021YFA0718700), CAS through the Youth Innovation Promotion Association (Grant No. 2022YSBR-048), the National Natural Science Foundation of China (Grants No. 11961141008, No. 11927808, and No. 12274439), the Key-Area Research and Development Program of Guangdong Province (Grant No. 2020B0101340002), and Beijing Natural Science Foundation (Grant No. Z190008).

- 
- [1] J. Bardeen, L. N. Cooper, and J. R. Schrieffer, Microscopic theory of superconductivity, *Phys. Rev.* **106**, 162 (1957).
  - [2] L. N. Cooper and D. Feldman, *BCS: 50 Years* (World Scientific, Singapore, 2010).
  - [3] J. Nagamatsu, N. Nakagawa, T. Muranaka, Y. Zenitani, and J. Akimitsu, Superconductivity at 39 K in magnesium diboride, *Nature (London)* **410**, 63 (2001).
  - [4] A. P. Drozdov, M. I. Erements, I. A. Troyan, V. Ksenofontov, and S. I. Shylin, Conventional superconductivity at 203 kelvin at high pressures in the sulfur hydride system, *Nature (London)* **525**, 73 (2015).
  - [5] X. Zhou, W. Lee, M. Imada, N. Trivedi, P. Phillips, H. Kee, P. Törmä, and M. Erements, High-temperature superconductivity, *Nat. Rev. Phys.* **3**, 462 (2021).
  - [6] Y. Li, W. Tabis, Y. Tang, G. Yu, J. Jaroszynski, N. Barišić, and M. Greven, Hole pocket-driven superconductivity and its universal features in the electron-doped cuprates, *Sci. Adv.* **5**, 7349 (2019).
  - [7] V. I. Sokolenko and V. A. Frolov, Topological electronic transition in cuprate high- $T_c$  superconductors occurring before the superconducting transition, *JETP Lett.* **105**, 661 (2017).
  - [8] S. Benhabib, A. Sacuto, M. Civelli, I. Paul, M. Cazayous, Y. Gallais, M. A. Méasson, R. D. Zhong, J. Schneeloch, G. D. Gu, D. Colson, and A. Forget, Collapse of the Normal-State Pseudogap at a Lifshitz Transition in the  $\text{Bi}_2\text{Sr}_2\text{CaCu}_2\text{O}_{8+\delta}$  Cuprate Superconductor, *Phys. Rev. Lett.* **114**, 147001 (2015).
  - [9] F. C. Chen, X. B. Bai, Y. X. Wang, T. Dong, J. N. Shi, Y. M. Zhang, X. M. Sun, Z. X. Wei, M. Y. Qin, J. Yuan, Q. H. Chen,

- X. B. Wang, X. Wang, B. Y. Zhu, R. J. Huang, K. Jiang, W. Zhou, N. L. Wang, J. P. Hu, Y. Li *et al.*, Emergence of superconducting dome in  $\text{ZrN}_x$  films via nitrogen manipulation, *Sci. Bull.* **68**, 674 (2023).
- [10] H. Tou, Y. Maniwa, T. Koiwasaki, and S. Yamanaka, Unconventional Superconductivity in Electron-Doped Layered  $\text{Li}_{0.48}(\text{THF})_y\text{HfNCl}$ , *Phys. Rev. Lett.* **86**, 5775 (2001).
- [11] Y. Kasahara, K. Kuroki, S. Yamanaka, and Y. Taguchi, Unconventional superconductivity in electron-doped layered metal nitride halides MNX ( $M = \text{Ti, Zr, Hf}$ ;  $X = \text{Cl, Br, I}$ ), *Physica C* **514**, 354 (2015).
- [12] B. W. Roberts, Survey of superconductive materials and critical evaluation of selected properties, *J. Phys. Chem. Ref. Data* **5**, 581 (1976).
- [13] Y. Zhu, M. Ikeda, Y. Murakami, A. Tsukazaki, T. Fukumura, and M. Kawasaki, Low-Temperature growth of highly crystalline superconducting zrn thin film on *c*-GaN layer by pulsed laser deposition, *Jpn. J. Appl. Phys.* **46**, L1000 (2007).
- [14] K. Tanabe, H. Asano, Y. Katoh, and O. Michikami, Properties of superconducting ZrN thin films deposited by dc reactive magnetron sputtering, *Jpn. J. Appl. Phys.* **26**, L570 (1987).
- [15] A. B. Mei, B. M. Howe, C. Zhang, M. Sardela, J. N. Eckstein, L. Hultman, A. Rockett, I. Petrov, and J. E. Greene, Physical properties of epitaxial ZrN/MgO (001) layers grown by reactive magnetron sputtering, *J. Vac. Sci. Technol. A* **31**, 061516 (2013).
- [16] S. Yamanaka, K. Hotehama, and H. Kawaji, Superconductivity at 25.5 K in electron-doped layered hafnium nitride, *Nature (London)* **392**, 580 (1998).
- [17] H. S. Seo, T. Y. Lee, J. G. Wen, I. Petrov, and J. E. Greene, Growth and physical properties of epitaxial HfN layers on MgO(001), *J. Appl. Phys.* **96**, 878 (2004).
- [18] H. Y. Tong, H. L. Zhang, Z. Z. Hui, X. W. Tang, R. H. Wei, W. H. Song, L. Hu, C. B. Cai, X. B. Zhu, and Y. P. Sun, Epitaxial superconducting  $\delta$ -MoN and  $\delta$ -NbN thin films by a chemical solution deposition, *J. Alloys Compd.* **826**, 154231 (2020).
- [19] J. H. Goldsmith, R. Gibson, T. Cooper, T. J. Asel, S. Mou, D. C. Look, J. S. Derov, and J. R. Hendrickson, Influence of nitride buffer layers on superconducting properties of niobium nitride, *J. Vac. Sci. Technol. A* **36**, 061502 (2018).
- [20] R. Schneider, B. Freitag, D. Gerthsen, K. S. Ilin, and M. Siegel, Structural, microchemical and superconducting properties of ultrathin NbN films on silicon, *Cryst. Res. Technol.* **44**, 1115 (2009).
- [21] W. M. Roach, J. R. Skuza, D. B. Beringer, Z. Li, C. Clavero, and R. A. Lukaszew, NbN thin films for superconducting radio frequency cavities, *Supercond. Sci. Technol.* **25**, 125016 (2012).
- [22] R. E. Treece, J. S. Horwitz, J. H. Claassen, and D. B. Chrisey, Pulsed laser deposition of high-quality NbN thin films, *Appl. Phys. Lett.* **65**, 2860 (1994).
- [23] Z. Wang, A. Kawakami, Y. Uzawa, and B. Komiyama, Superconducting properties and crystal structures of single-crystal niobium nitride thin films deposited at ambient substrate temperature, *J. Appl. Phys.* **79**, 7837 (1996).
- [24] D. Hazra, N. Tsavdaris, S. Jebbari, A. Grimm, F. Blanchet, F. Mercier, E. Blanquet, C. Chapelier, and M. Hofheinz, Superconducting properties of very high quality NbN thin films grown by high temperature chemical vapor deposition, *Supercond. Sci. Technol.* **29**, 105011 (2016).
- [25] K. Il'in, M. Hofherr, D. Rall, M. Siegel, A. Semenov, A. Engel, K. Inderbitzin, A. Aeschbacher, and A. Schilling, Ultra-thin tan films for superconducting nanowire single-photon detectors, *J. Low Temp. Phys.* **167**, 809 (2012).
- [26] K. Wakasugi, M. Tokunaga, T. Sumita, H. Kubota, M. Nagata, and Y. Honda, Superconductivity of reactivity sputtered TaN film for ULSI process, *Physica B* **239**, 29 (1997).
- [27] R. Mencia, Y. H. Lin, and V. Manucharyan, Superconducting titanium nitride films grown by directional reactive evaporation, *J. Appl. Phys.* **130**, 225109 (2021).
- [28] C. J. K. Richardson, A. Alexander, C. G. Weddle, B. Arey, and M. Olszta, Low-loss superconducting titanium nitride grown using plasma-assisted molecular beam epitaxy, *J. Appl. Phys.* **127**, 235302 (2020).
- [29] U. S. Pracht, M. Scheffler, M. Dressel, D. F. Kalok, C. Strunk, and T. I. Baturina, Direct observation of the superconducting gap in a thin film of titanium nitride using terahertz spectroscopy, *Phys. Rev. B* **86**, 184503 (2012).
- [30] J. F. Zasadzinski, A. Saggese, K. E. Gray, R. T. Kampwirth, and R. Vaglio,  $T^4$  to  $T^2$  resistivity transition and superconducting fluctuations in disordered VN films, *Phys. Rev. B* **38**, 5065 (1988).
- [31] K. E. Gray, R. T. Kampwirth, D. W. Capone, II, R. Vaglio, and J. Zasadzinski, Superconducting properties of  $\text{VN}_x$  sputtered films including spin fluctuations and radiation damage of stoichiometric VN, *Phys. Rev. B* **38**, 2333 (1988).
- [32] H. L. Luo, S. A. Wolf, W. W. Fuller, A. S. Edelstein, and C. Y. Huang, Superconductivity of VN under pressure, *Phys. Rev. B* **29**, 1443 (1984).
- [33] Š. Huber, O. Jankovský, D. Sedmidubský, J. Luxa, K. Klímová, J. Hejtmánek, and Z. Sofer, Synthesis, structure, thermal, transport and magnetic properties of VN ceramics, *Ceram. Int.* **42**, 18779 (2016).
- [34] L. B. Wang, Z. S. Lou, K. Y. Bao, W. Q. Liu, and Q. F. Zhou, Low-temperature solid state synthesis and characterization of superconducting vanadium nitride, *Chin. Phys. Lett.* **34**, 028101 (2017).
- [35] A. Cassinese, M. Iavarone, R. Vaglio, M. Grimsditch, and S. Uran, Transport properties of ZrN superconducting films, *Phys. Rev. B* **62**, 13915 (2000).
- [36] C. Moura, P. Carvalho, F. Vaz, L. Cunha, and E. Alves, Raman spectra and structural analysis in  $\text{ZrO}_x\text{N}_y$  thin films, *Thin Solid Films* **515**, 1132 (2006).
- [37] M. A. Signore, A. Rizzo, L. Mirengghi, M. A. Tagliente, and A. Cappello, Characterization of zirconium oxynitride films obtained by radio frequency magnetron reactive sputtering, *Thin Solid Films* **515**, 6798 (2007).
- [38] J. Guo, G. H. Zhan, J. Q. Liu, B. Yang, B. Xu, J. Feng, X. Chen, and C. S. Yang, Hopping conduction in zirconium oxynitrides thin film deposited by reactive magnetron sputtering, *Physica B* **475**, 86 (2015).
- [39] G. H. Zhan, J. Q. Liu, J. Guo, J. Feng, B. Xu, B. Yang, X. Chen, and C. S. Yang, Electrical transport property of zirconium oxynitride thin film deposited by magnetron sputtering process, *J. Mater. Sci.: Mater. Electron.* **26**, 9188 (2015).
- [40] X. M. Sun, X. B. Bai, F. C. Chen, R. J. Huang, J. Yuan, K. Jin, H. J. Su, and L. F. Li, Influence of magnetron sputtering process parameters on low temperature electrical transport characteristics of zirconium oxynitride thin films, *IOP Conf. Series: Mater. Sci. Eng.* **1241**, 012052 (2022).



- [41] J. Wu, Z. Li, L. Peng, Y. Yi, and J. Zhang, Metal-insulator transition in zirconium oxynitride films, *Physica B* **624**, 413428 (2022).
- [42] P. Carvalho, F. Vaza, L. Rebouta, L. Cunha, C. J. Tavares, and C. Moura, Structural, electrical, optical, and mechanical characterizations of decorative  $\text{ZrO}_x\text{N}_y$  thin films, *J. Appl. Phys.* **98**, 023715 (2005).
- [43] K. C. Lan, J. H. Huang, C. F. Ai, and G. P. Yu, Structure and properties of nanocrystalline  $\text{ZrN}_x\text{O}_y$  thin films: Effect of the oxygen content and film thickness, *J. Vac. Sci. Technol. A* **29**, 031506 (2011).
- [44] I. Krylov, V. Korchnoy, X. B. Xu, K. Weinfeld, E. Yalon, D. Ritter, and M. Eizenberg, Electrical and structural properties of conductive nitride films grown by plasma enhanced atomic layer deposition with significant ion bombardment effect, *J. Appl. Phys.* **128**, 065301 (2020).
- [45] B. Keimer and J. E. Moore, The physics of quantum materials, *Nat. Phys.* **13**, 1045 (2017).
- [46] A. W. Tsien, B. Hunt, Y. D. Kim, Z. J. Yuan, S. Jia, R. J. Cava, J. Hone, P. Kim, C. R. Dean, and A. N. Pasupathy, Nature of the quantum metal in a two-dimensional crystalline superconductor, *Nat. Phys.* **12**, 208 (2016).
- [47] N. R. Werthamer, E. Helfand, and P. C. Hohenberg, Temperature and purity dependence of the superconducting critical field,  $H_{c2}$ . III. electron spin and spin-orbit effects, *Phys. Rev.* **147**, 295 (1966).
- [48] A. Gurevich, Enhancement of the upper critical field by non-magnetic impurities in dirty two-gap superconductors, *Phys. Rev. B* **67**, 184515 (2003).
- [49] F. Hunte, J. Jaroszynski, A. Gurevich, D. C. Larbalestier, R. Jin, A. S. Sefat, M. A. McGuire, B. C. Sales, D. K. Christen, and D. Mandrus, Two-band superconductivity in  $\text{LaFeAsO}_{0.89}\text{F}_{0.11}$  at very high magnetic fields, *Nature (London)* **453**, 903 (2008).
- [50] X. M. Sun, X. B. Bai, F. C. Chen, R. J. Huang, W. Wang, J. Yuan, K. Jin, and L. F. Li, Preparation of  $\text{ZrO}_x\text{N}_y$  thin films and research on low-temperature electrical transport properties, *Cryogenics* **1**, 31 (2022).
- [51] M. Yoshizawa, K. Ikeda, H. Sugawara, N. Toyota, T. Yotsuya, and M. Yoshitake, Electrical resistivity and high-field magnetoresistance of Zr-N film thermometers, *Jpn. J. Appl. Phys.* **31**, 2472 (1992).
- [52] Q. Zhang, K. Jiang, Y. H. Gu, and J. P. Hu, Unconventional high temperature superconductivity in cubic zinc-blende transition metal compounds, *Sci. China: Phys., Mech. Astron.* **63**, 277411 (2020).